Non-linear dynamics of a rotor system with compliant seal

Simon Bäuerle*, Hartmut Hetzler*

Engineering Dynamics Group, Institute of Mechanics, University of Kassel, Kassel, Germany

Summary. New so-called hybrid seals have recently been developed combining advantages of labyrinth and brush seals. This contribution discusses one of their properties by investigating the influence of compliant seal support on rotordynamic behaviour. The model under investigation consists of a *Laval*-rotor (*Jeffcott*-rotor) and a visco-elastically supported stiff seal ring. The non-linear *Muszynska*-model is applied to represent the fluid forces stemming from the turbulent flow through the seal. The system dynamics are investigated for an unbalanced and the special case of a balanced rotor. In both cases, stability and bifurcation analysis is conducted. Due to the compliant support equilibrium or periodic solutions exist at higher rotational speeds compared with a stiff seal support. Unbalance leads to stabilisation- and synchronisation-effects. Resonance passage is possible with a lowered risk of rotor-seal contact. A rich bifurcation and non-linear behaviour is encountered after the steady state solutions loose their stability.

Introduction

Seals are important components for a lot of machinery. By reducing leakage they secure machine function and maintain efficiency. In rotating machinery design solutions are needed that seal the necessary gap between rotating and standing parts: Labyrinth or brush seals are frequently used in this case. Nonetheless, even seemingly simple elements like seals produce new design challenges: one example is today's demand for variable operation schemes for conventional power plants due to fluctuating generation of renewable energy that require seals to be capable of adapting to turbine rotor vibrations induced by the more frequently occurring start-up and shut-down runs [1].

Labyrinth seals are comparatively inexpensive standard functional elements which are being used since decades with a broad application range. The contact-free working principle causes almost no wear and leads to a long service life under ideal working conditions. Aiming for low leakage characteristics the sealing gap is kept as small as possible but at the same time it must be able to compensate rotor vibrations and thermal expansion without surface contact. The ever remaining leakage flow leads to fluid forces and inherent circulatory forces: above a distinctive operational speed a loss of steady-state stability might be the result with consequences reaching from unwanted noise emission or increased leakage due to seal damage up to material fatigue.

Brush seals are in contrast contacting seals comprising fibres which are usually made out of metal in a housing. The densely packed brush can reportedly reduce the leakage up to 60% [2] to 80% [1] (in a multistage variant) compared to a conventional labyrinth seal whilst being able to adapt to rotor deflection [3]. In addition, the fibre structure breaks up fluid swirl [2], which is a physical mechanism behind destabilising circulatory forces [4]. Apart from thermally induced rotor vibrations due to frictional heating between rotor surface and bristles (Newkirk-effect [5, 6]), leakage induced instabilities are thus far less likely to occur. Yet, brush seals are more expensive and their function principle inherits shorter maintenance and replacement intervals.

A comparatively new approach are compliant hybrid seals (e.g. HALO seal [7], GLAND seal [1], hybrid brush seals [3]). The idea of various designs is to combine the advantages of labyrinth and brush seals: non-contacting surfaces lead to low wear while added flexibility in the seal structure gives the capacity to adapt to rotor deflection and therefore minimizing the risk of surface rubbing. The adaptability makes it possible to define smaller sealing gaps in the construction process, therefore lowering leakage and increasing efficiency. In addition, HALO and GLAND seal adjust the gap according to the pressure drop over the seal and the pressure distribution in the seal. HALO seals are already in use and can reduce leakage up to 70% compared to labyrinth seals [7].

An important part in modelling the influence of seals on rotordynamics is the description of the lubrication flow. The high pressure drop leads to high axial velocities and most of the time turbulent flow. Whilst fully- or semi-coupled multibody-CFD simulations are always possible they are most of the time too costly. This is why modelling approaches often restrict themselves using reduced fluid flow models which is permissible due to the large aspect ration between rotor radius and sealing gap. Literature provides a lot of different turbulent flow models applicable at intermediate Reynolds-numbers, like the *Constantinescu* model from 1959 [8] or the *Ng-Pan* model from 1965 [9], and flow models for higher Reynolds-numbers when omitted fluid inertia is not allowed. Popular representatives are the extended *Constantinescu*-[10] and *Ng-Pan*-models [11] or the semi-empirical *Hirs*-model [12]. In fact, the mentioned models are just some popular representatives and new mathematical flow descriptions are still developed today.

Most often, even doing coupled simulation with lower dimensional PDE models is still too cumbersome. This is the reason why it's common practice in rotordynamics to use force coefficient ODE models for the fluid forces stemming from seals, which are usually dependent on the rotor position and the rotational speed. These (non-linear) dependencies and the case specific coefficients are either determined by experiment, numerical integration of a reduced model or the *Navier-Stokes* equation or analytical description. Here, we use *Muszynska's* model [13, 14, 15] to describe the mathematical structure. *Muszynska* postulated the mentioned non-linear dependencies of the fluid forces based on heuristic considerations as well as experimental and numerical observations. The bulk-flow theory is the basis for the modelling approach: since the sealing gap is small compared to the rotor radius any radial flow can approximately be neglected. The remaining variables are substituted by radially averaged quantities. The result is a fluid bulk co-rotating in the sealing gap with an averaged

angular velocity of $0 < \tau_{f0}\Omega < \frac{1}{2}\Omega$, where $\tau_{f0} = \frac{1}{2}$ is the radial mean value of a perfect laminar *Couette*-flow. This has the interpretation of a fluid force rotating with $\tau_{f0}\Omega$ for the case of a centred shaft. In addition to that, the model relies on the following conditions to hold [14] : The rotor vibrations must be small enough for the circumferential flow to remain unidirectional (no secondary/ backward flow) and the whole flow must be temporally fully developed. The model has been widely used in literature not only by *Muszynska* herself who investigated oil whirl and whip phenomena [13] but also to look into non-linear rotordynamic phenomena like bifurcations, complicated periodic orbits and chaotic behaviour [16, 17, 18, 19]. To account for the coefficients of the ODE model *Childs'* equations [4] based on *Hirs'* bulk flow model [12] are used. *Childs'* looked at small perturbations of a rotor spinning centric in a short seal and derived analytical expressions for the coeffcients of a linear ODE describing the fluid forces.

The objective of this contribution is to investigate the non-linear dynamic behaviour of a rotor system with a compliant seal considering a balanced as well as an unbalanced rotor. In the modelling section the compliant rotor-seal model is presented and the *Muszynska* model is discussed. The results section is subdivided into two parts: The first one presents the stability and non-linear behaviour of a balanced system whereas the second part does the same for the unbalanced case. The contribution closes with a summary and outlook. All results were obtained using MATLAB® and/or the continuation toolbox MATCONT.

Nomenclature			
subscripted R/S: rotor/seal-related,		A : matrix $\quad a$: column-matrix $\quad \vec{a}$: vector	
$\mathcal{I}$: inertially fixed cartesian reference frame		$\mathcal{R}$: rotor fixed/ co-rotating cartesian reference frame	
$\vec{q}_{R,S} = \frac{\vec{q}_{R,S}}{C}$	dimensionless position vector wrt $\mathcal{R}$	t	time
$\bar{q}_{R,S} = \frac{\bar{q}_{R,S}}{C}$	dimensionless position matrix wrt $\mathcal{R}$	C	nominal sealing gap
q_0	equilibrium position wrt $\mathcal{R}$	D_f/D_{f0}	fluid damping
$\Delta\vec{q} = \vec{q}_R - \vec{q}_S$	dimensionless rotor seal distance wrt $\mathcal{R}$	K_f/K_{f0}	fluid stiffness
$\vec{r}_{R,S} = \frac{\vec{r}_{R,S}}{C}$	dimensionless position vector wrt $\mathcal{I}$	L	seal length
$\bar{r}_{R,S} = \frac{\bar{r}_{R,S}}{C}$	dimensionless position matrix wrt $\mathcal{I}$	R	rotor radius
$\Delta\vec{r} = \vec{r}_R - \vec{r}_S$	dimensionless rotor seal distance wrt $\mathcal{I}$	V	axial fluid speed through seal
$\vec{F}_f(\Delta\vec{r}) = \frac{\vec{F}_f}{c_R C}$	dimensionless fluid force wrt $\mathcal{I}$	$\delta_{R,S} = \frac{d_{R,S}}{2\sqrt{c_{R,S}m_{R,S}}}$	dimensionless rotor damping constant
$B_{(),R,S}$	general/ rotor/ seal matrix of velocity proportional forces	$\delta_f/\delta_{f0} = \frac{D_f/D_{f0}}{2\sqrt{c_R m_R}}$	dimensionless fluid damping/ constant
$C_{(),R,S}$	general/ rotor/ seal matrix of positional proportional forces	$\varepsilon = \|\vec{q}_R - \vec{q}_S\|$	relative eccentricity
$M_{(),R,S}$	general/ rotor/ seal mass matrix	$\eta = \frac{\Omega}{\omega_R}$	dimensionless angular rotor speed
Q	matrix defined by equation (13)	$\kappa^2 = \frac{c_S}{c_R}$	stiffness ratio
R	rotation matrix	$\kappa_f^2/\kappa_{f0}^2 = \frac{K_f/K_{f0}}{c_R}$	dimensionless fluid stiffness/ constant
$\bar{T} = \frac{1}{\eta}$	dimensionless period duration	μ	dynamic fluid viscosity
b	empirical parameters	$\mu_S^2 = \frac{m_S}{m_R}$	seal mass ration
$c_{R,S}$	stiffness coefficient	$\mu_f^2 = \frac{m_f}{m_R}$	fluid mass ratio
$d_{R,S}$	damping coefficient	ξ	seal inlet pressure loss coefficient
e	mass eccentricity	ρ	fluid density
m_f	coefficient of fluid inertia	$\tau = \omega_R t$	dimensionless time
$m_{R,S}$	rotor/ seal mass	τ_f/τ_{f0}	fluid average circumferential velocity ratio/ constant
m_0	*Childs-Hirs* coefficient [4]	$\Delta\varphi$	phase difference between rotor and seal
n	empirical parameters	$\omega_R = \frac{c_R}{m_R}$	rotor eigenfrequency
n_0	*Childs-Hirs* coefficient [4]	Ω	angular rotorspeed
Δp	pressure drop over seal		

Table 1: Nomenclature of used variables and parameters.

Used abbreviation					
EQ	equilibrium position	PLC	periodic limit cycle	QPLC	quasi-periodic limit cycle
FB	fold bifurcation	HB	*Hopf* bifurcation	NSB	*Neimark-Sacker* bifurcation
SFB	secondary fold bifurcation/ fold bifurcation for maps	SNSB	secondary *Neimark-Sacker* bifurcation/ *Neimark-Sacker* bifurcation for maps		

Table 2: Abbreviations used in the results chapter.

Specific parameter values			
b = 0.5	n_0 = 0.066	R = $15 \cdot 10^{-2}$ m	μ_S^2 = 0.25
c_R = $7.92 \cdot 10^4 \frac{\text{N}}{\text{m}}$	Δp = $6 \cdot 10^5 \frac{\text{N}}{\text{m}^2}$	δ_R = 0	ξ = 0.5
m_R = 50 kg	C = $0.005 \cdot R$	δ_S = 0.05	ρ = 1000 $\frac{\text{kg}}{\text{m}^3}$
m_0 = -0.25	L = $0.1 \cdot R$	μ = $1.295 \cdot 10^{-3} \frac{\text{Ns}}{\text{m}^2}$	τ_0 = 0.45
n = 2			

Table 3: Specific parameter values used for simulation.

Modelling
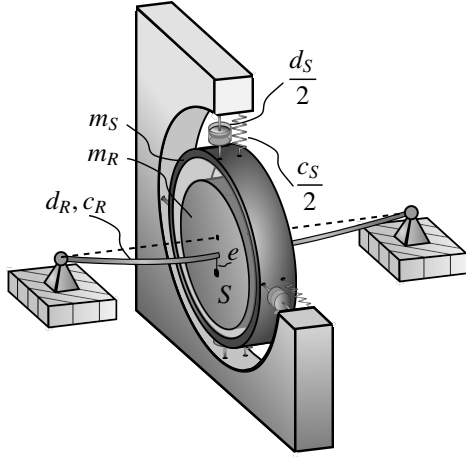
Figure 1: Minimal model consisting of a *Laval*-rotor, a stiff seal ring (visco-elastically connected to its surrounding) and an incompressible turbulent fluid flow streaming the gap between the two bodies.

The minimal model used for the investigation is shown in figure 1 and consists of three parts: The first part is a classical *Laval*-rotor where the centre of mass S has a mass eccentricity e. It rotates with the constant dimensionless angular velocity $\eta = \frac{\Omega}{\omega_R}$. The stiff seal ring is the second part: It is visco-elastically connected to its inertially fixed surrounding whereby this support allows only for translative motions. The two rigid bodies move solely in-plane and their physical properties are indicated in figure 1. Introducing an inertial cartesian system $\mathcal{I}$ one can describe the dynamical behaviour by the dimensionless equations

$$\underbrace{\begin{bmatrix} 1 & 0 \\ 0 & 1 \end{bmatrix}}_{:=M_R} \vec{r}_R'' + \underbrace{\begin{bmatrix} 2\delta_R & 0 \\ 0 & 2\delta_R \end{bmatrix}}_{:=B_R} \vec{r}_R' + \underbrace{\begin{bmatrix} 1 & 0 \\ 0 & 1 \end{bmatrix}}_{:=C_R} \vec{r}_R = \frac{e}{C}\eta^2 \begin{pmatrix} \cos(\eta\tau) \\ \sin(\eta\tau) \end{pmatrix}_{\mathcal{I}} + \vec{F}_f(\Delta\vec{r}) \quad (1)$$

and

$$\underbrace{\begin{bmatrix} \mu_S^2 & 0 \\ 0 & \mu_S^2 \end{bmatrix}}_{:=M_S} \vec{r}_S'' + \underbrace{\begin{bmatrix} 2\mu_S\kappa\delta_S & 0 \\ 0 & 2\mu_S\kappa\delta_S \end{bmatrix}}_{:=B_S} \vec{r}_S' + \underbrace{\begin{bmatrix} \kappa^2 & 0 \\ 0 & \kappa^2 \end{bmatrix}}_{:=C_S} \vec{r}_S = -\vec{F}_f(\Delta\vec{r}) \quad (2)$$

$$\text{where} \quad \Delta\vec{r} = \vec{r}_R - \vec{r}_S \quad (3)$$

and $(.)' = \frac{\text{d}}{\text{d}\tau}$ being the derivation with respect to the dimensionless time τ.

Within this investigation the influence of gravitational forces is not considered. The forces $\vec{F}_f(\Delta\vec{r})$ originate from the third part: an incompressible, newtonian, turbulent lubrication film. It is driven by the pressure drop Δp over the seal and the rotation $\eta\tau$ of the rotor. The resulting fluid forces act on seal and rotor and are described by the non-linear *Muszynska*-model which states

$$\vec{F}(\Delta\vec{r}) = -\underbrace{\begin{bmatrix} \mu_f^2 & 0 \\ 0 & \mu_f^2 \end{bmatrix}}_{:=M_f} \Delta\vec{r}'' - \underbrace{\begin{bmatrix} 2\delta_f & 2\tau_f\mu_f^2\eta \\ -2\tau_f\mu_f^2\eta & 2\delta_f \end{bmatrix}}_{:=B_f} \Delta\vec{r}' - \underbrace{\begin{bmatrix} \kappa_f^2 - \left(\tau_f\mu_f\eta\right)^2 & \tau_f\delta_f\eta \\ -\tau_f\delta_f\eta & \kappa_f^2 - \left(\tau_f\mu_f\eta\right)^2 \end{bmatrix}}_{:=C_f} \Delta\vec{r} \quad (4)$$

for the dimensionless force depending only on the relative displacement $\Delta\vec{r}$. Furthermore,

$$\kappa_f^2 = \kappa_{f0}^2(1 - \|\vec{r}_R - \vec{r}_S\|^2)^{-n}, \quad (5) \qquad \delta_f = \delta_{f0}(1 - \|\vec{r}_R - \vec{r}_S\|^2)^{-n} \quad (6) \qquad \text{and} \qquad \tau_f = \tau_{f0}(1 - \|\vec{r}_R - \vec{r}_S\|^2)^b \quad (7)$$

are defined. The parameters μ_f^2, δ_{f0}^2 and κ_{f0}^2 are determined using *Childs* analytical formulas [4] for short plain seals. These formulas are based on *Hirs'* bulk flow theory which only guarantees good agreement to experiments for an axial *Reynolds*-number $R_a = \frac{\rho LVC}{\mu} < 10^5$ and satisfactory agreement for a circumferential *Reynolds*-number $R_c = \frac{\rho R\eta\omega_R}{\mu} < 10^5$ [20]. These numbers are reached at a angular velocity of about $\eta = 30$ which will be the upper boundary for all subsequent considerations. Equation (5) and (6) underline an important limitation of the *Muszynska*-model: If the dimensionless distance between rotor and seal centre (relative eccentricity $\varepsilon = \|\vec{r}_R - \vec{r}_S\|$) approaches 1, dimensionless stiffness coefficient κ_f and dimensionless damping coefficient δ_f tend to infinity since $n = 2$ was assumed (cf. table 3). Subsequently, this modelling does not permit contact between rotor and seal which is clearly unphysical. Thus, the relative eccentricity is not allowed to take on values close to 1.

Condensing these formulas into a compact notation one obtains

$$
\overbrace{\begin{bmatrix} M_R + M_f & -M_f \\ -M_f & M_S + M_f \end{bmatrix}}^{:=M} \begin{bmatrix} \vec{r}_R{}'' \\ \vec{r}_S{}'' \end{bmatrix} + \overbrace{\begin{bmatrix} B_R + B_f(\Delta\vec{r}) & -B_f(\Delta\vec{r}) \\ -B_f(\Delta\vec{r}) & B_S + B_f(\Delta\vec{r}) \end{bmatrix}}^{:=B} \begin{bmatrix} \vec{r}_R' \\ \vec{r}_S' \end{bmatrix} +
$$

$$
+ \underbrace{\begin{bmatrix} C_R + C_f(\Delta\vec{r}) & -C_f(\Delta\vec{r}) \\ -C_f(\Delta\vec{r}) & C_S + C_f(\Delta\vec{r}) \end{bmatrix}}_{:=C} \begin{bmatrix} \vec{r}_R \\ \vec{r}_S \end{bmatrix} = \frac{e}{C}\eta^2 \begin{bmatrix} \begin{pmatrix} \cos(\eta\tau) \\ \sin(\eta\tau) \end{pmatrix}_{\mathcal{I}} \\ \begin{pmatrix} 0 \\ 0 \end{pmatrix}_{\mathcal{I}} \end{bmatrix}. \quad (8)
$$

Investigating oscillations induced by unbalance, it is favourable to rewrite equations (8) with respect to a cartesian coordinate system $\mathcal{R}$, which rotates with the angular velocity η and with co-rotating coordinates

$$\bar{r}_R = R q_R \quad (9) \qquad \text{and} \qquad \bar{r}_S = R q_S \quad (10) \qquad \text{where} \qquad R = \begin{bmatrix} \cos(\eta\tau) & -\sin(\eta\tau) \\ \sin(\eta\tau) & \cos(\eta\tau) \end{bmatrix}. \quad (11)$$

Since $\|\vec{r}_R - \vec{r}_S\|^2 = \|\vec{q}_R - \vec{q}_S\|^2$ holds, inserting equations (9) to (11) into equations (8) gives

$$
M \begin{bmatrix} \vec{q}_R{}'' \\ \vec{q}_S{}'' \end{bmatrix} + (B(\Delta\vec{q}) - 2\eta Q M) \begin{bmatrix} \vec{q}_R' \\ \vec{q}_S' \end{bmatrix} + \left(K(\Delta\vec{q}) - \eta Q B(\Delta\vec{q}) - \eta^2 M \right) \begin{bmatrix} \vec{q}_R \\ \vec{q}_S \end{bmatrix} = \frac{e}{C}\eta^2 \begin{bmatrix} \begin{pmatrix} 1 \\ 0 \end{pmatrix}_{\mathcal{R}} \\ \begin{pmatrix} 0 \\ 0 \end{pmatrix}_{\mathcal{R}} \end{bmatrix} \quad (12)
$$

where

$$Q = \begin{bmatrix} \begin{bmatrix} 0 & 1 \\ -1 & 0 \end{bmatrix} & \mathbf{0} \\ \mathbf{0} & \begin{bmatrix} 0 & 1 \\ -1 & 0 \end{bmatrix} \end{bmatrix}. \quad (13)$$

The transformation leads to autonomous differential equations where equilibrium solutions unequal to zero correspond to circular (harmonic) rotor and seal limit cycles with a period duration of $\bar{T} = \frac{1}{\eta}$.

Results

Balanced *Laval*-rotor:
Analysis of stability behaviour
Figure 3 shows a stability chart, where the stiffness ratio $\kappa^2 = \frac{c_R}{c_S}$ is plotted against the angular speed η. The chart displays the results of the eigenvalue computation of the perturbation equations corresponding to equations (8), linearised around the trivial solution. The encircled digits indicate the number of unstable eigenvalues present in the areas separated by a solid black or grey dashed lines. The letters A and B correspond each to a specific pair of complex conjugated eigenvalues with positive real parts. The black dot-dashed line is the stability limit of a system with a stiff seal support.
Three interesting conclusions can be drawn: Firstly, the visco-elastic seal support leads to an increased parameter range with stable solutions. This range is the area between the dot-dashed black and the solid black line.
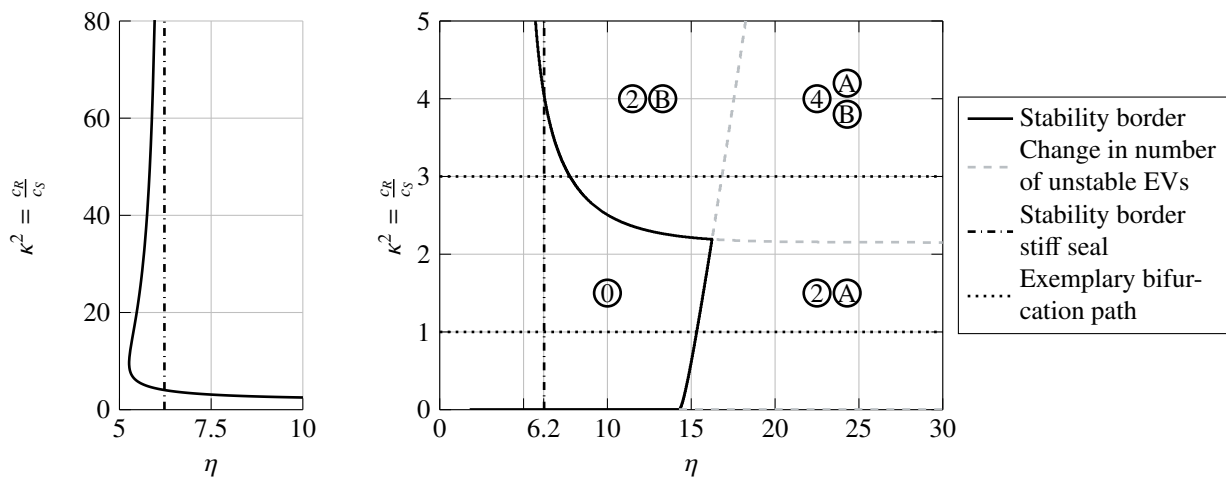
Figure 2: In κ−direction extended plot detail from figure 3.

Figure 3: Steady state stability chart in dependence of stiffness ratio κ^2 and dimensionless angular rotor speed η. Encircled digits indicate areas with noted numbers of unstable eigenvalues; encircled letters A and B correspond to a specific pair of eigenvalues with positive real parts. Source: [21].

Secondly, the movability of the seal stabilizes the solution: the stability limit for compliant support approaches the limit for stiff support with increasing support stiffness and converges to it for higher κ values (see figure 2) where the seal is less movable. And thirdly, the solutions become unstable due to different complex conjugated eigenvalue pairs: pair A in the upper left area differs from pair B in the lower right area thereby affecting the shape of the stability limit and leading to characteristic non-linear behaviour. Both of these pairs have positive real parts in the upper right area.

Analysis of bifurcation behaviour
The qualitative bifurcation behaviour can be represented by two exemplary bifurcation paths: Figure 4 and 5 show the evolution of radii $\|\vec{r}_{R,S}\|$ of the circular orbits of rotor and seal with the bifurcation parameter η for $\kappa^2 = 1$ and $\kappa^2 = 3$ (marked by grey dotted lines in figure 3). Here, solid black lines indicate stable circular seal (dotted) and rotor orbits. Dashed light grey lines mark unstable circular seal (dotted) and rotor orbits. The (un)stable equilibrium states are represented by (dashed) grey lines. In figure 4 the steady state solutions loose their stability via a *Hopf* bifurcation. It occurs when the complex conjugates eigenvalue pair A attains positive real parts. The seal exhibits medium sized amplitudes whilst the rotor only displays comparatively small ones: a continued operation after the loss of stability might be possible. Time simulation reveals that rotor and seal always move synchronised with a relative phase difference of about π. Figure 5 on the other hand shows a completely different solution behaviour. Again, the steady state solution looses its stability via a *Hopf* bifurcation but in this instance due to the eigenvalue pair B. Rotor and seal display large amplitudes both being bigger than the sealing gap C. This is only possible since both rigid bodies move synchronised with almost no phase difference. The magnitude of the amplitude would most certainly prohibit ongoing operation. Raising the bifurcation parameter η further the periodic cycles loose their stability via a *Neimark-Sacker* bifurcation. Crossing the area of the unstable eigenvalue pair A to the area of A and B in figure 3 an unstable periodic orbit emerges which gains its stability via a *Neimark-Sacker* bifurcation. Please note the qualitative similarity between these limit cycles and the ones for $\kappa^2 = 1$. The two *Neimark-Sacker* points are connected by an quasi-periodic repellor (mean radius indicated by light grey dashed line). The repellor was approximated by time integration with initial conditions chosen from the subspace defined by the linearised centre manifold of the associated *Poincaré* map. *Fast Fourier Transformation* of the quasi-periodic orbits of rotor and seal in the neighbourhood of the repellor reveals again synchronised behaviour.
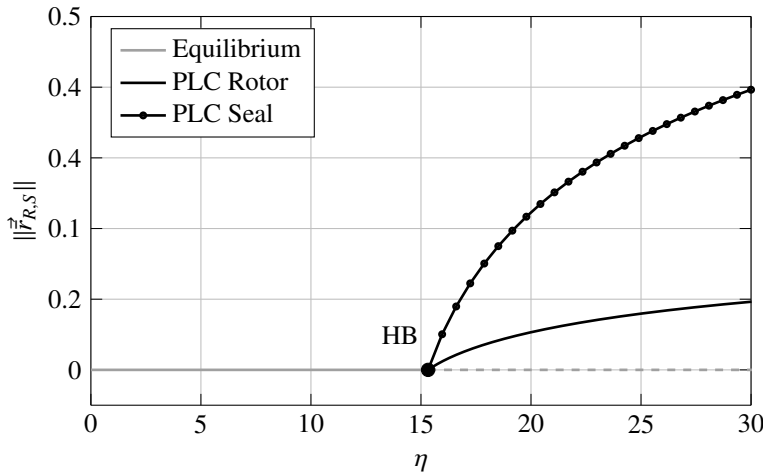
Figure 4: Bifurcation plot: steady states and circular limit cycles radii $\|\vec{r}_{R,S}\|$ over dimensionless angular rotor velocity η for $\kappa^2 = 1$. Solid lines: stable solutions; dashed lines: unstable solutions.
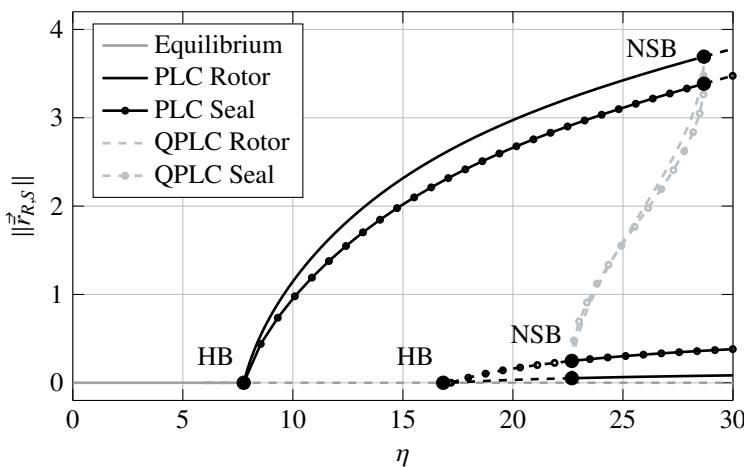
Figure 5: Bifurcation plot: steady states and circular limit cycles radii $\|\vec{r}_{R,S}\|$ over dimensionless angular rotor speed η for $\kappa^2 = 3$. Solid lines: stable solutions; dashed lines: unstable solutions; light grey dashed lines: mean radius of quasi-periodic repellor.

Unbalanced *Laval*-Rotor:
Unbalance is always present in rotating parts and can have a major influence on the system at least for increased rotational speeds. In the present case the mass eccentricity leads to periodic limit cycles of rotor and seal which can also become unstable: quasi periodic motions are in general the subsequent result. The stability behaviour can be investigated by help of the *Floquet* theory. Nevertheless, it is favourable to investigate the occurring phenomena in the co-rotating coordinate system $\mathcal{R}$. In this subsection all terminology refers to system $\mathcal{R}$ followed by the corresponding expression referring to the inertially fixed reference frame $\mathcal{I}$ in brackets (used abbreviations cf. table 2)

Analysis of stability behaviour

In co-rotating coordinates the stability investigation of periodic limit cycles reduces to an eigenvalue analysis of equilibria. Therefore, the perturbation equations corresponding to (12) are linearised around the equilibrium position $\boldsymbol{q}_0$ defined in reference-frame free notation by

$$\left(\boldsymbol{K}(\Delta \boldsymbol{q}_0) - \eta \boldsymbol{Q}\boldsymbol{B}(\Delta \boldsymbol{q}_0) - \eta^2 \boldsymbol{M}\right) \boldsymbol{q}_0 = \frac{e}{C}\eta^2 \begin{bmatrix} 1 \\ 0 \\ 0 \\ 0 \end{bmatrix} \tag{14}$$

being dependent on the angular speed η, the stiffness ratio κ and the mass eccentricity e. Results of the computation can be seen in figure 6 where different grey shadings correspond to the indicated mass eccentricities. The numerical computation of these charts is way more costly than for the unbalanced case with up to 20 hours per chart on a standard desktop computer for a straight-forward high resolution scanning of eigenvalues. An efficient pseudo-arc-length continuation has been used instead cutting computation time to under 20 minutes. For very small mass eccentricities the stability limit coincides with the limit for the balanced case in figure 3. Increasing the mass eccentricity entails two interesting effects: On the one hand side the stability area is enlarged which is an effect also seen on *Laval*-rotors with inner damping and unbalance. On the other hand side tongues of extended stability develop when e is raised. Possible explanations will be discussed later on.

Figure 8 displays exemplarily the stability chart for $e = 0.15\,C$. The encircled digits indicate the number of unstable eigenvalues (*Floquet* multipliers) present in the separated areas. The letters C and D correspond each to a specific pair of complex conjugated eigenvalues with positive real parts (*Floquet* multipliers with a norm greater than one). The black dot-dashed line is the stability limit of a system with a stiff seal support. Apart from the mentioned stability tongue a very similar behaviour to the balanced case is encountered: The stability limit for compliant seal support converges towards the limit for a stiff support with increasing stiffness ratio κ (cf. figure 7) which emphasises also in the unbalanced case the movability of the seal as the stabilizing mechanism. Please note, that the stability limit for stiff support for an unbalanced system also lies considerably higher than the limit for the balanced counterpart, which is in accordance with the findings for the compliant system. In addition to that, solutions become again unstable due to different eigenvalue pairs (*Floquet* multipliers) leading to characteristic bifurcation behaviour.

Figure 6: Stability chart for unbalanced induced equilibria (PLC) in dependence of stiffness ratio κ^2 and dimensionless angular rotor speed η for different mass eccentricities.

Analysis of bifurcation behaviour

Again, two exemplary bifurcation paths are investigated for $\kappa^2 = 1$ and $\kappa^2 = 7$ in order to assess the bifurcation behaviour. They are indicated in figure 8.

The path for $\kappa^2 = 1$ is shown in figure 9 and will be discussed in two parts: In the section between $\eta = 0$ and the marked *Hopf* bifurcation (NSB) grey dotted or solid lines correspond to equilibrium positions of seal or rotor. The dash-dotted line shows the course of the relative eccentricity $\varepsilon = \|\vec{q}_R - \vec{q}_S\|$ where a value of 1 means contact between rotor and seal. The equilibrium positions correspond to stationary periodic orbits therefore indicating the amplification function for rotor and seal with two resonance peaks. At the first peak for $\eta = 1.25$ high, but bounded values occur ($\|\vec{q}_{R,S}\| \approx 4$, excluded due to purpose of presentation). However, the relative eccentricity shows that only medium-sized relative displacements exist: Rotor and seal are unlikely to touch each other despite passage through the resonance. This is a big advantage for operation purposes. Interpreting with respect to the inertially fixed reference frame $\mathcal{I}$, we see that the relevant eigenvector corresponding to the critical eigenvalue at the second resonance peak for $\eta = 6.25$ leads to an amplification of seal and reduction of rotor amplitudes. These values settle to more or less medium-sized positions of rotor and seal. The seemingly non-correlated development of the relative eccentricity is explained by the phase difference between seal and rotor: It changes from an in-phase motion even during the first resonance to a phase difference of $\Delta\varphi \approx \frac{2}{3}\pi$.
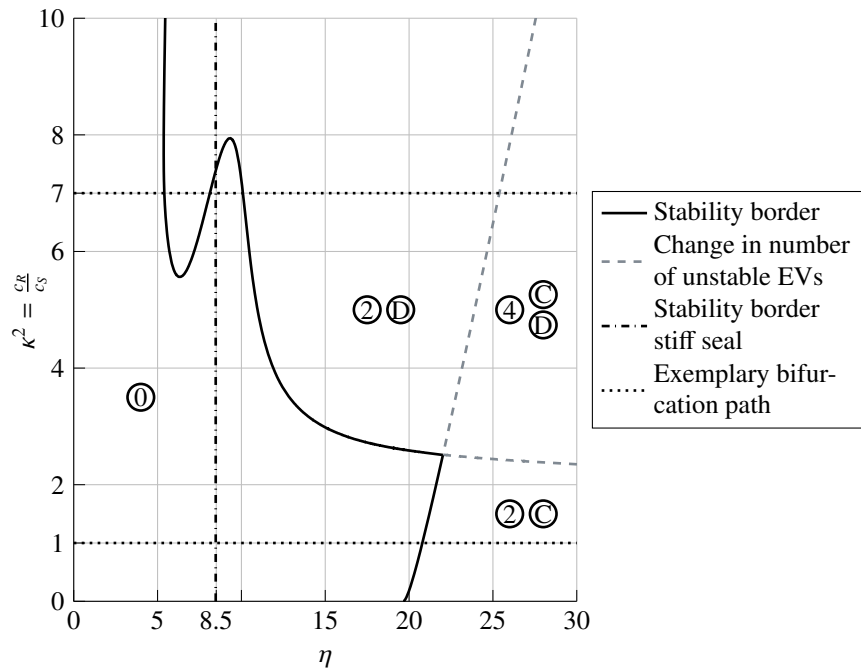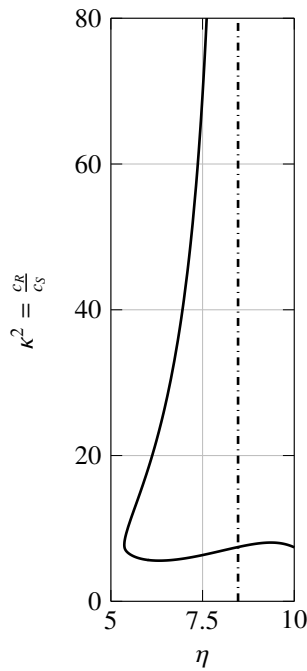
Figure 7: In κ−direction extended plot detail from figure 8.

Figure 8: Stability chart for unbalanced induced equilibria (PLC) in dependence of stiffness ratio κ^2 and dimensionless angular rotor speed η for $e = 0.15\,C$. Encircled digits indicate areas with noted numbers of unstable eigenvalues (*Floquet* multipliers); encircled letters C and D correspond to a specific pair of eigenvalues (*Floquet* multipliers) with positive real parts (norm greater than one).

The second part relates to the section on the right of the *Hopf* bifurcation (NSB). Here, the dashed or solid grey lines indicate the unstable seal or rotor equilibrium (PLC). Dotted or solid black lines refer to the amplitudes $\|\vec{q}_{R,S}\|$ of the evolving limit cycles (QPLC). When the solutions on bifurcation path 1 cross the solid black line in figure 8 a *Hopf* bifurcation (NSB) occurs and the equilibrium (PLC) looses its stability. The solution in coordinate system $\mathcal{I}$ moves then on a 2-torus. Rotor and seal amplitudes stay comparatively bounded although the seal amplitudes evolve rapidly. Qualitative resemblance with the amplitude progression for the balanced case in figure 4 is present.
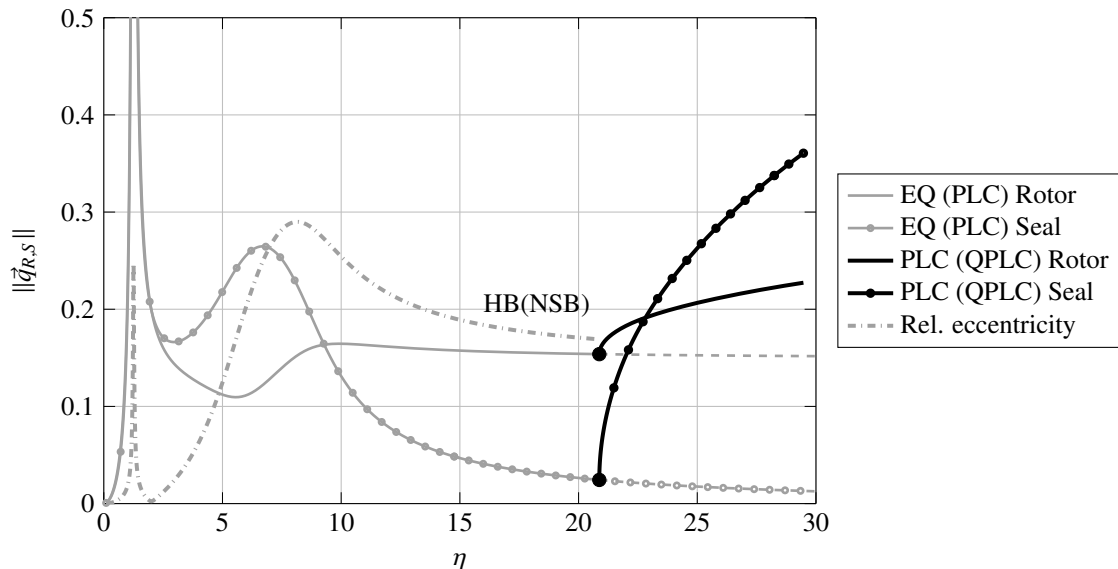
Figure 9: Amplification and bifurcation plot: equilibria (PLCs) and circular limit cycles radii $\|\vec{q}_{R,S}\|$ over dimensionless angular rotor speed η for $\kappa^2 = 1$. Solid lines: stable solutions; dashed lines: unstable solutions.

The second bifurcation path is shown in figure 10 and an appropriate plot detail in figure 11. The course of the equilibrium position (PLC) is apart from the stability properties qualitatively analogues to the one seen in figure 9. The same statement is true for the course of the relative eccentricity ε (cf. figure 11). Nevertheless, there are two connected quantitative differences: Firstly, the height of the first resonance peak is reduced by a factor of approximately two. And secondly, the relative eccentricity displays much larger values in the same area. The explanation is given by the interaction between

stiffness ration, seal and fluid damping: For the chosen parameter configuration the relation for the fluid damping to the seal damping $\delta_f \approx 10\,\delta_S$ holds (rotor damping $\delta_R = 0$). At $\kappa^2 = \frac{c_S}{c_R} = 1$ the seal support stiffness is comparatively low and thus the seal easy to move. The fluid compression or respectively the relative eccentricity is low and therefore the fluid damping. The large seal movement has no influential contribution to the overall system damping due to the low constant δ_S. At $\kappa^2 = \frac{c_S}{c_R} = 7$ the seal movability is considerably diminished: the relative eccentricity rises. The process is now dominated by the much higher fluid damping. The overall damping rises and limits the maximal resonance amplitudes.
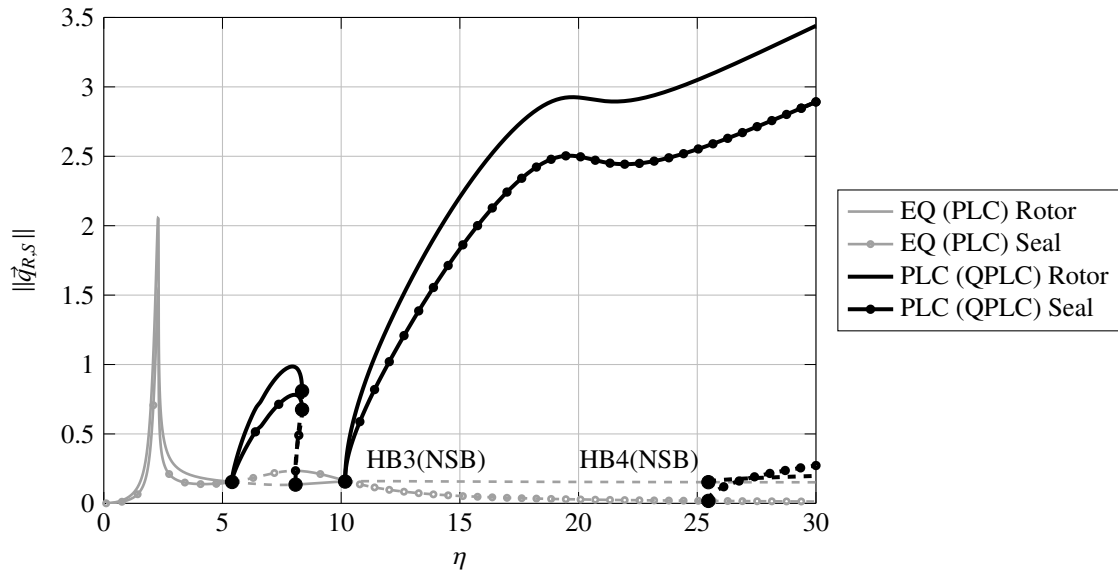
Figure 10: Amplification and bifurcation plot: equilibria (PLCs) and circular limit cycles radii $\|\vec{q}_{R,S}\|$ over dimensionless angular rotor speed η for $\kappa^2 = 7$. Solid lines: stable solutions; dashed lines: unstable solutions.

Yet, the main differences to figure 9 are the two instability areas. We will now discuss four parts separately.
The first instability of the equilibrium (PLC) occurs between the first and second *Hopf* bifurcation (NSB) (cf. figure 11). The solution looses its stability and displays a periodic limit cycle (QPLC) with fast rising amplitudes for seal and rotor. The orbit then looses for itself stability in a fold bifurcation (SFB) much like in the well known non-linear resonance curve of a *Duffing* oscillator. The stability is gained again in a fold bifurcation (SFB) and the limit cycles (QPLC) merges with the equilibrium position (PLC) in *Hopf* bifurcation 2 (NSB) (both bifurcations are in close proximity and not shown separately). Four solutions coexist in the $\eta-$interval limited by the corresponding *Hopf* bifurcation 2 (NSB) and the lower fold bifurcation (SFB).
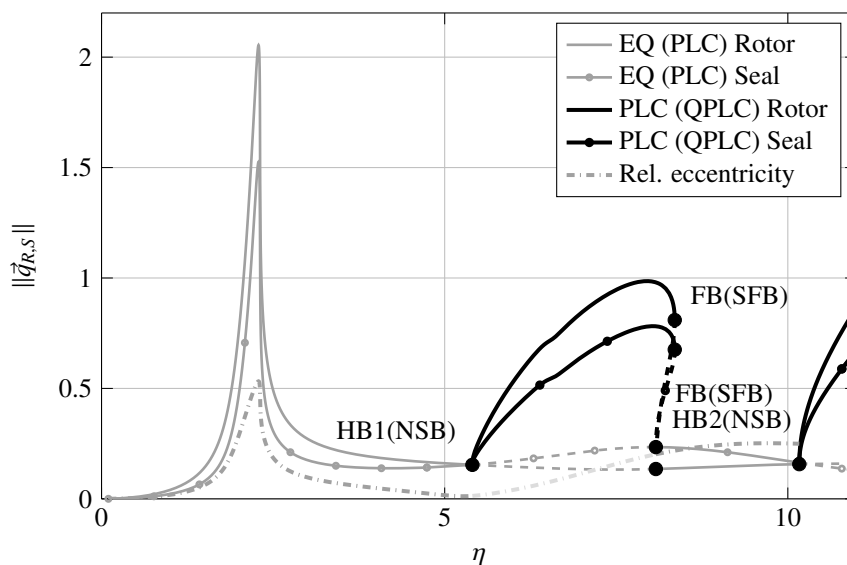
Figure 11: Amplification and bifurcation plot: plot detail from figure 10.

The second part to be discussed is the interval of the retrieved equilibrium stability (PLC) between the second and third *Hopf* bifurcation (NSB) (cf. figure 11). In fact, the extended stability tongues in figure 6 are areas of synchronisation between the fluid-induced self-excited vibrations and the vibrations due to unbalance. These tongues correspond in their growth with the mass eccentricity to the areas of elevated seal amplitudes due to the second resonance. Looking at figure 10 the synchronisation point coincides most interestingly nearly exactly with the resonance peak of the seal amplitude. A growing synchronisation area can be caused by an increasing external (unbalance) excitation like in the textbook example of an externally forced *van-der-Pol* oscillator [22]. However, the rotor amplitude drops in this case in the synchronisation area which is also not symmetric to the second resonance.

A possible explanation might be the influence of the relative eccentricity (dashed-dotted grey line): Approaching the synchronisation area with rising η, the relative eccentricity increases leading to higher fluid damping. The raise in damping might suppress the self-excited oscillations thus synchronising the system. In addition to that the system is due to the coefficient dependency on η not symmetric around the resonance peak.

The third part is the periodic limit cycle starting from *Hopf* bifurcation 3 (cf. figure 10). Two interesting aspects are worth noting: On the one hand, the amplitudes rise very fast very high. This will most certainly prohibit an ongoing operation. On the other hand, the qualitative course of the amplitudes is comparable to the limits cycle (QPLC) between *Hopf* bifurcation 2 and 3: The same eigenvectors D become unstable here being characteristic for the qualitative development. The fourth part are the unstable limit cycles (QPLC) starting from *Hopf* bifurcation 4. Here again, comparable behaviour due to the same eigenvector C becoming unstable can be found in bifurcation path 1 in figure 9. Especially the section between *Hopf* bifurcation 3 and $\eta = 30$ shows good qualitative resemblance with the second bifurcation path of the balanced system in figure 5. Due to this obvious analogy it can be assumed that the unstable limit cycles (QPLC) will gain their stability in a *Neimark-Sacker* bifurcation (SNSB). Coexisting limit cycles (QPLC) will then be separated by a 3-torus repellor. However, this behaviour is beyond the validity of the used fluid force model for the coefficients.

Conclusion and Outlook

Hybrid seals represent a new design direction with promising potential. In this contribution a simple model of a rotor system with compliant seal properties has been investigated. The case of a balanced and unbalanced rotor have been discussed whereby the latter one is of more practical relevance. Compliant support or more specifically the enabled movability of the seal ring has been shown to lead to an increased stable operation range depending on parameter values. Raised mass eccentricities lead to a further stabilisation as well as the formation of stability tongues with synchronised behaviour. For an unbalanced rotor the relative eccentricity, which is the distance between rotor and seal centre stays bounded and rather small even in case of elevated amplitudes. Therefore, safe resonance passage is enabled. Solution stability is lost in either *Hopf* or *Neimark-Sacker* bifurcations. Ongoing operation thereafter can be possible depending on the stiffness ratio between seal support and rotor stiffness. Unstable periodic solutions might loose and regain their stability in *Neimark-Sacker* or fold bifurcations. Stable periodic solutions can be separated by quasi-periodic repellors.

Future work comprises three major parts: An extended investigation of non-linear effects of the present model with focus on synchronisation and the non-linear behaviour after a loss of stability (*Arnold* tongues, chaos) will be conducted, which requires a fluid model with validity for higher rotational speeds. The second part is a fully coupled FEM simulation of *Hirs'* fluid model in order to gain a deeper understanding for the fluid mechanical influence and to verify the force coefficient models used in this contribution. Yet unpublished work has already been done in this area. And the third major part is the construction and commissioning of a test rig, which is in progress.

References

[1] Messenger A. et al. (2015) A dynamic clearance seal for steam turbine application *ASME Turbo Expo 2015* V008T26A031-V008T26A031.

[2] Pugachev, A. O. and Deckner, M. (2010) CFD prediction and test results of stiffness and damping coefficients for brush-labyrinth gas seals *ASME Turbo Expo 2010: Power for Land, Sea, and Air* 175-185.

[3] Chupp R. E., Hendricks R. C., Lattime S. B. and Steinetz, B. M. (2006) Sealing in turbomachinery *J Propul Power* 22(2): 313-349.

[4] Childs D. W. (1983) Dynamic analysis of turbulent annular seals based on Hirs' lubrication equation *J Lubric Tech-T ASME* 105.3: 429-436.

[5] Dimarogonas, A.D. (1973) Newkirk effect: thermally induced dynamic instability of high-speed rotors *In ASME 1973 International Gas Turbine Conference and Products Show* V001T01A026-V001T01A026.

[6] Fay, R., Kreuzer, D. and Liebich, R. (2014) The Influences of thermal effects induced by the light-rub against the brush seal to the rotordynamics of turbo machines *ASME Turbo Expo 2014: Turbine Technical Conference and Exposition* V07AT31A008-V07AT31A008.

[7] San Andrés L. et al. (2015) An all-metal compliant seal versus a labyrinth seal *J. Eng. Gas Turb. Power* 137 1–8.

[8] Constantinescu VN. (1967) The pressure equation for turbulent lubrication *Institution of Mechanical Engineering: Proceedings of the Conference on Lubrication and Wear* 182: 183 ff.

[9] Ng CW. and Pan CHT. (1965) A linearized turbulent lubrication theory *J. Basic Eng.* 87(3): 675-682.

[10] Constantinescu VN. (1970) On the influence of inertia forces in turbulent and laminar self-acting film *J Lubric Tech-T ASME* 92(3): 473-480.

[11] Pan, CHT. (1974) Calculation of pressure, shear, and flow in lubricating films for high speed bearings *J Lubric Tech-T ASME* 96(1): 80-94.

[12] Hirs G. G. (1973) A bulk-flow theory for turbulence in lubricant films *J Fluid Struct* 95(2): 137-145.

[13] Muszynska A. (1986) Whirl and whip – rotor/bearing stability problems. *J. Sound Vib.* 110.3: 443–462.

[14] Przekwas A. J., Muszynska A., Hendricks R. C., Braun M. J. and Mullen R. L. (1988) Numerical and analytical study of fluid dynamic forces in seals and bearings *J Vib Acoust* 110: 315-325.

[15] Muszynska A. (1988) Improvements in lightly loaded rotor/bearing and rotor/seal models *J Vib Acoust* 110(2): 129-135.

[16] Song-tao L., Qing-yu X., Fang-yi W. and Xiao-long Z. (2003) Stability and bifurcation of unbalance rotor/labyrinth seal system, *Appl Math Mech* 24(11): 1290-1301.

[17] Ding Q., Cooper JE and Leung AYT. (2002) Hopf bifurcation analysis of a rotor/seal system *J Sound Vib*, 252(5) 817-833.

[18] Cheng M., Meng G., Jing J.P. (2007) Numerical study of a rotor-bearing-seal system *Proceedings of the Institution of Mechanical Engineers: Part C, H Mech Eng Sci* 221(7): 779-788.

[19] Li S., Xu Q., Zhang, X. (2007) Nonlinear dynamic behaviors of a rotor-labyrinth seal system *Nonlinear Dynam* 47.4: 321-329.

[20] Hirs G. G. (1970) Fundamentals of a bulk-flow theory for turbulent lubricant films *Delft University Holland*.

[21] Baeuerle S., Hetzler H. (2016) Bifurcation behaviour and limit cycles of a compliant seal-rotor system *PAMM* 16.1: 257-258.

[22] Jordan D. and Smith P. (2007) Nonlinear ordinary differential equations: an introduction for scientists and engineers *Oxford University Press*.